DOI: 10.13009/EUCASS2023-585
Aerospace Europe Conference 2023 – 10TH EUCASS – 9TH CEAS

Wind Tunnel Characterization of a Delta-Wing UAV for Model-Based Navigation

Pasquale Longobardi[⋆†]*, Guillaume Bonneau*[⋆] *and Jan Skaloud*[⋆]
[⋆]*EPFL Laboratory of Cryospheric Sciences*
Route des Ronquos 86, 1950 Sion Switzerland
pasquale.longobardi@epfl.ch, jan.skaloud@epfl.ch
[†]Corresponding author

Abstract

This paper presents an experimental procedure for aerodynamic characterization of a delta-wing UAV for model-based navigation applications. We report the design of experiments, aimed to maximize aerodynamic coefficients observability while meeting time constraints requirements, as well as the significance of secondary aerodynamic influences. A functional model, simple yet accurate, is derived from the experiments. We evaluate it empirically in-flight with an offline-implemented navigation solution during GNSS-signal outages, using data exclusively collected from low-cost sensors embedded in a commercially available autopilot. Results showed that the model-based navigation solution produced a significantly smaller positioning error compared to traditional navigation approaches during GNSS outage.

1. Introduction

Vehicle Dynamic Model (VDM) based navigation is a relatively recent approach to autonomous navigation that, contrary to the traditional kinematic approach, leverages geometrical information about the adopted vehicle. By utilizing the knowledge of the vehicle's functional model structure and the precise numerical values of its parameters, VDM-based navigation offers several advantages. This navigation approach is particularly effective in situations where the vehicle relies on an IMU[1] with a sensor of lower precision than tactical grade and operates in environments where GNSS[2] signals are unreliable or unavailable. Small UAVs often incorporate lower-grade IMUs, to meet weight and cost constraints, and are subject to GNSS outages when operating in constricted environments. They have thus become one of the potential targets for this technology. Simulations [6] and empirical testing [7] [8] on a small drone of a conventional aircraft with 4 (3-independent) control surfaces have shown considerable improvements in localization (an order of magnitude or more) compared to inertial coasting. However, this type of platform is seldom used for purposes different than recreational flying or research purposes. Delta-wing UAVs and rotorcrafts each present advantages over conventional aircraft UAVs. Rotorcrafts possess the ability to hover and to move omnidirectionally which makes them great products for inspection missions. However, their flight mechanism relies on a power utilization approach that is less optimal, resulting in limited flying endurance. Delta-wing UAVs, conversely, maximize payload capacity by only sustaining flight with a pair of additional wings, offering a more efficient use of available space with respect to aircrafts of conventional shape and rotorcrafts. Their geometry, based on a lower Aspect Ratio due to the wing sweep, enhances structural rigidity and lowers the sensitivity to Reynolds number [14]. Furthermore, this class of platforms exhibits significantly enhanced flight autonomy which makes it the ideal platform for mapping/photogrammetry applications where large portions of terrain need to be scanned within a single flight. As a result, the objective of this work is the determination of an aerodynamic model to implement model-based navigation for a delta-wing UAV obtaining the aforementioned improvements in navigation. To accomplish this objective, a meticulously designed set of experiments was conducted using an open wind-tunnel experimental set-up.
The remainder of this paper is organized as follows: Section 2 provides the necessary foundational concepts and theoretical framework of this study. It outlines the adopted navigation filter architecture, the model formulation for UAV body aerodynamics and propulsion system, and the secondary aerodynamic effects examined in this study. Section 3 describes the open wind tunnel experimental set-up, with details on the hardware utilized during the experiments. Section 4 highlights the methodology employed for the collection of the aerodynamic data. Notably, it presents the

[1]Inertial Measurement Unit
[2]Global Navigation Satellite System

DOI: 10.13009/EUCASS2023-585

theory behind the chosen data sampling technique and the functional model identification methodology from collected data. The results are discussed in detail in Section 5 where the experimental data for both the UAV body and propulsion system are analysed in conjunction with secondary aerodynamic effects, such as propwash and Reynolds number effect. Additionally, the autonomous navigation performance of the resulting vehicle model is evaluated during GNSS outage conditions, and is subsequently compared to a traditional kinematic navigation solution based on inertial sensing. Finally Section 6 provides a summary of this study's primary contribution and discusses the significance and implications of the findings.

2. Theoretical Framework

2.1 Model-based Navigation Filter Architecture

The model-based navigation filter architecture employed is shown in Figure 1.

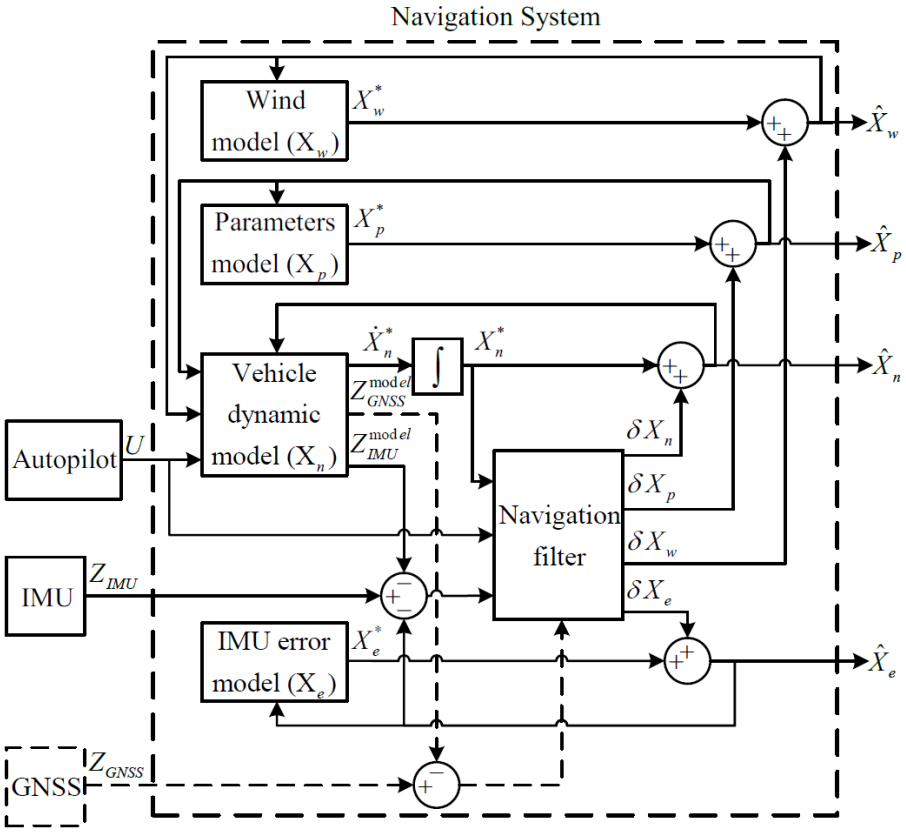

Figure 1: VDM-based navigation filter architecture. *Image courtesy [6]*

This architecture reflects the implementation proposed by Khaghani et al. [6] where the vehicle dynamic model is implemented as the navigation filter process model, fed by autopilot control commands. IMU and GNSS measurements are simply treated as observations. The filter augmented state vector contains the navigation solution Xn, the actuator states Xa, the aerodynamic characterization of the platform Xp, the stochastic parameters of the modeled sensor errors Xe, and, finally, the wind components Xw. A more detailed depiction of the model-based filter architecture and its equations is provided in [6].

2.2 Platform Aerodynamic Model

The core of the UAV dynamics is the aerodynamic model, which provides the prediction of forces and moments perceived by the platform as a consequence of flight parameters, i.e. angle of attack α and side slip angle β, control parameters, i.e. control surface deflection, and dynamic parameters, i.e. angular velocities ω_x, ω_y and ω_z.
Delta-wing UAVs only rely on two control surfaces, placed on the wing, which are called elevons and whose independent deflections are symbolized with α_L and α_R. In this work, α_L is the deflection of the left elevon and it is positive

DOI: 10.13009/EUCASS2023-585

when going up, α_R is the right elevon deflection which is positive when going down. The action of elevons within the aerodynamic model is expressed as a combination of symmetrical deflection, or elevator effect δ_e, and asymmetrical deflection, or aileron effect δ_a, which are mathematically defined as follows:

$$\delta_a = \frac{\alpha_L - \alpha_R}{2}, \quad \delta_e = \frac{\alpha_L + \alpha_R}{2} \tag{1}$$

The forces, respectively called drag D, side force Y, and lift L, are defined in the wind frame, depicted in Figure 2. This frame has its first axis in the direction of the airspeed vector V and describes two angles with respect to the first axis of the UAV body frame: angle of attack α in the longitudinal plane and angle of side-slip β in the lateral plane. The moments acting on the platform are instead expressed in the body frame, which is depicted in the same figure, and take respectively the name of roll moment M_x, pitch moment M_y, and yaw moment M_z.

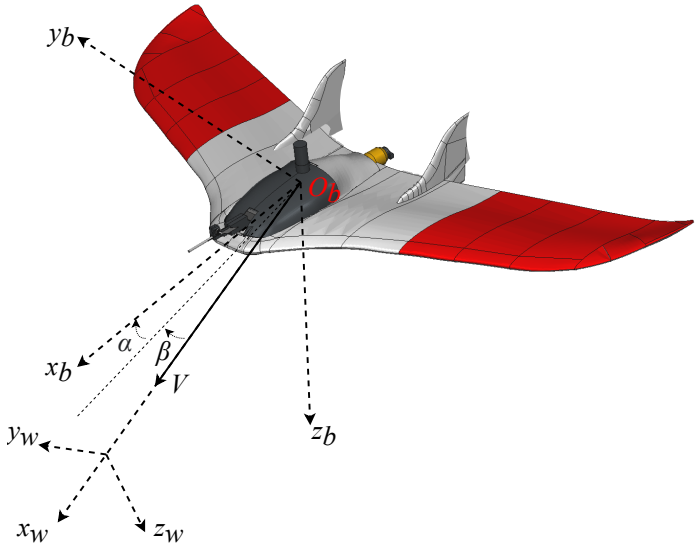

Figure 2: Wind frame and related flight parameters with respect to the platform body frame.

In the absence of platform-specific model structure information, the navigation filter process model relies on a generalized formulation that decouples longitudinal and lateral dynamics and incorporates all flight, control and dynamic parameters [3]. The equations for such a model are presented as follows:

$$C_D = C_{D0} + C_{D\alpha}\alpha + C_{D\alpha 2}\alpha^2 + C_{D\beta}\beta + C_{D\delta_e}\delta_e + C_{D\omega_x}\omega_x + C_{D\omega_y}\omega_y + C_{D\omega_z}\omega_z \tag{2}$$

$$C_Y = C_{Y\beta}\beta + C_{Y\beta 2}\beta^2 + C_{Y\delta_a}\delta_a + C_{Y\omega_x}\omega_x + C_{Y\omega_y}\omega_y + C_{Y\omega_z}\omega_z \tag{3}$$

$$C_L = C_{L0} + C_{L\alpha}\alpha + C_{L\alpha 2}\alpha^2 + C_{L\beta}\beta + C_{L\delta_e}\delta_e + C_{L\omega_x}\omega_x + C_{L\omega_y}\omega_y + C_{L\omega_z}\omega_z \tag{4}$$

$$C_{Mx} = C_{M_{x\beta}}\beta + C_{M_{x\beta 2}}\beta^2 + C_{M_{x\delta_a}}\delta_a + C_{M_{x\omega_x}}\omega_x + C_{M_{x\omega_x}}\omega_x + C_{M_{x\omega_z}}\omega_z \tag{5}$$

$$C_{My} = C_{My0} + C_{My\alpha}\alpha + C_{My\alpha 2}\alpha^2 + C_{My\beta}\beta + C_{My\delta_e}\delta_e + C_{My\omega_x}\omega_x + C_{My\omega_y}\omega_y + C_{My\omega_z}\omega_z \tag{6}$$

$$C_{Mz} = C_{M_{z\beta}}\beta + C_{M_{z\beta 2}}\beta^2 + C_{M_{z\delta_a}}\delta_a + C_{M_{z\omega_x}}\omega_x + C_{M_{z\omega_x}}\omega_x + C_{M_{z\omega_z}}\omega_z \tag{7}$$

However, this model structure is not optimized for the employed UAV platform and results in an increased state space within the navigation filter, leading to higher computational requirements.
Common approaches to model structure and corresponding aerodynamic coefficient identification involve traditional wind tunnel testing or the use of CFD (Computational Fluid Dynamics) software. Unfortunately, these approaches can be both time-consuming and expensive. The objective is hence the determination of experimental procedures that allow to identify an aerodynamic model accurate enough while minimizing the time required for data acquisition.
In Section 4 , a detailed description will be provided outlining the experimental design implemented in order to accomplish the stated objective.

DOI: 10.13009/EUCASS2023-585

2.3 Propulsion Model

Following the same aerodynamic characterization detailed in [1] the thrust and the torque are modeled as follows:

$$T(J,\omega) = C_{T0} \cdot \rho \cdot D^4 \cdot \omega^2 + C_{T1} \cdot \rho \cdot D^4 \cdot J \cdot \omega^2 \quad (8)$$

$$Q(J,\omega) = C_{Q0} \cdot \rho \cdot D^5 \cdot \omega^2 + C_{Q1} \cdot \rho \cdot D^5 \cdot J \cdot \omega^2 \quad (9)$$

Where ρ indicates the air density and D the propeller diameter. The adimensional quantity $J = V/\omega D$ is the advance ratio and contains the true airspeed V and propeller rotation speed ω.
The coefficients C_{T0}, C_{T1} for the thrust model and C_{Q0}, C_{Q1} for the torque model are experimentally derived in Section 5.3.

2.4 Secondary Aerodynamic Effects

In the following are discussed the principal secondary aerodynamic effects considered for this study, namely the *Reynolds number* and *propwash effects*.

2.4.1 Reynolds number effect

The Reynolds number is a dimensionless parameter defined as:

$$Re = \frac{\rho V L}{\mu} \quad (10)$$

Where L indicates the characteristic length of the system, V the airspeed magnitude, ρ and μ respectively the density and viscosity of the medium. It represents the relative importance of inertial forces compared to the viscous ones of the airflow. For an aircraft, the chord-based Reynolds number ($Re_c = \rho V \bar{c}/\mu$) is most often used, where the characteristic length of the system adopted is the airfoil's mean aerodynamic chord $\bar{c}$. Fixed the platform ($\bar{c}$) and the air condition (density ρ and viscosity μ) the Reynolds number only depends on the airspeed magnitude V.
The Reynolds number defines whether the airflow regime around the UAV body is laminar, turbulent, or a mixture of both and, in the case of the latter, in which proportion. This information impacts the aerodynamic behavior of the platform. In particular, this quantity is relevant for a small-sized UAV where the Reynolds number is in the order of 10^5 and it is close to its critical value as there is an important shift in airfoil performance when the Reynolds number decreases below 300 000 [4]. When in this range, a lower airspeed translates to a specific flying regime, while a higher airspeed may indicate a different regime.
In Section 5.1.3 we analyse the significance of this secondary aerdynamic effect for the platform under exam.

2.4.2 Propwash effect

The propwash effect describes the influence a spinning propeller has on the airflow distribution around the UAV body. This interaction is dependent on the placement of the propeller, either ahead or behind the center of gravity, referred to as a tractor or pusher propeller, respectively.
Thipyopas et al. [12] investigated, via wind tunnel testing, the influence of propulsion-induced flows on longitudinal dynamics for a fixed-wing MAV with a tractor propeller. They found that the propeller locally enhanced the airflow velocity around the MAV body while simultaneously reducing the actual angle of attack. Consequently, the lift coefficient (C_L) decreased due to the reduction in alpha outweighing the increase in local speed. On the other hand, the drag coefficient (C_D) exhibited no clear trend at higher Reynolds numbers but showed a more significant impact at lower values, indicating an additional propwash drag. The mutual interaction between a pusher propeller and the airframe is numerically (CFD) investigated in [2], which concluded that a rotating propeller can significantly affect the drag coefficient, with the increase in fuselage drag dependent on the motor RPMs. In a wind tunnel experimental study conducted by Traub [13], the effect of a pusher propeller on a delta wing was analyzed. Pusher configuration causes delay in vortex breakdown (which are the cause of the stall) increasing lift at higher alpha.
It is worth noting that the propwash effect caused by a tractor propeller is generally more pronounced than that caused by a pusher propeller, as downstream airflow alteration has a greater impact than upstream action [5]. As a result,most of the existing literature focuses on examining the propwash effect induced by tractor propellers. However, this study focuses on a platform configuration featuring a pusher propeller. Hence, it is necessary to experimentally characterize the propwash effect specific to the examined platform. Section 5.3.1 of this paper will discuss the experimental findings concerning the propwash effect, providing insights into its characteristics and implications for the final aerodynamic characterization.

DOI: 10.13009/EUCASS2023-585

3. Experimental Set-up

The experiments have been carried out at the open-wind tunnel experimental facility of the Laboratory of Intelligent Systems at EPFL. The set-up is depicted in Figure 3 and consists of four main components: i) a wind generator, called Windshaper [10], ii) a robotic arm to continuously change the orientation of the UAV with respect to the airstream, iii) a 6-axis load cell to measure forces and torques and iv) a motion capture system to monitor the UAV's attitude.

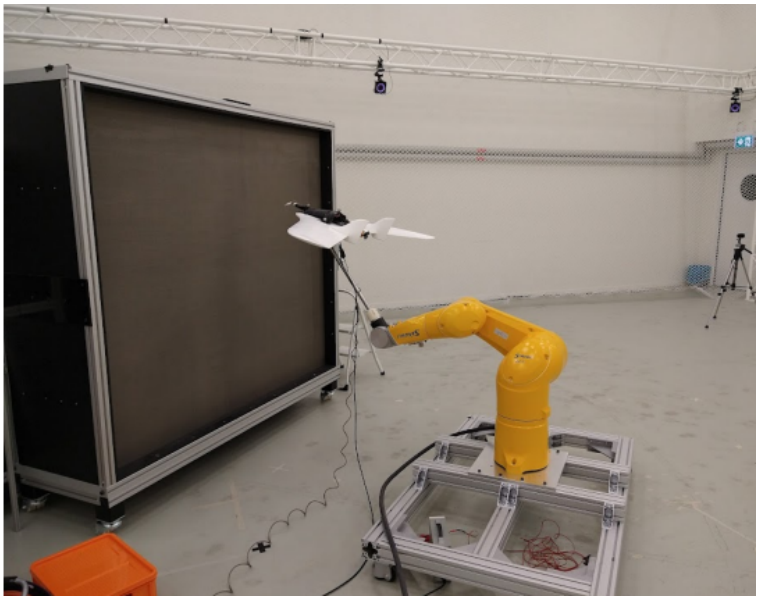

Figure 3: Experimental set-up.

A custom delta-wing UAV, developed at the Geodetic Engineering Laboratory, EPFL, is tested in the afore-described facility. The prototyping of this UAV platform involved modifying the body of a hobby product (Xeno Electric from Multiplex[3]) to accommodate a larger payload, containing autopilot and different sensors, and upgrading its power-train system to sustain the augmented take-off weight. The employed autopilot is a PixHawk 4 Holybro running a customized version of the open-source software PX4 (firmware version FMU-v5). A high-end multi-frequency GNSS receiver and antenna, an airspeed sensor, an angle of attack vane, and an RPM sensor were integrated into the platform and are connected to the autopilot.
The propulsion system is constituted by a fixed-pitch propeller actuated by a brushless direct current (BLDC) motor controlled via an electric speed controller (ESC). The control command to the ESC arrives as a PWM signal issued by the PixHawk autopilot. The thrust and the torque produced by the spinning propeller are measured using the previously introduced 6-axis load cell whereas the motor RPMs are obtained using the aforementioned RPM sensor, connected to the ESC, that provides its measurements to the autopilot.

4. Methodology

The Delta-wing platform is connected to the 6-axis load cell placed at the end of the robotic arm. The objective of the experiments is to isolate and identify the aerodynamic response of the Delta-wing platform to changes in flight, control and dynamic parameters. The robotic arm is programmed to follow a specific trajectory, describing the sequence of attitudes the drone must take during the experiment. The elevons are individually controlled to generate different combinations of control commands. The load cell measures the total force and moment perceived by the UAV as a result of its interaction with the airflow generated by the Windshaper. The measurements obtained by the load cell include three main components: i) aerodynamic interaction, ii) gravity, and iii) inertial components caused by linear/angular acceleration. As the objective is to isolate the aerodynamic interaction, the first component needs to be separated from the others. To achieve this, the experiments are performed twice; the first experiment is conducted without any wind (no-wind experiment), whereas the second experiment involves generating a desired reference airflow using the Windshaper (wind experiment). The measurements obtained in the no-wind experiment are then aligned via cross-correlation and subtracted from the measurements obtained in the wind experiment. As the gravity and inertial

[3] https://www.multiplex-rc.de/

DOI: 10.13009/EUCASS2023-585

components would be the same in both experiments, this subtraction eliminates their combined effects, thereby yielding the required aerodynamic forces and moments.

4.1 Data Sampling

Proper planning of the experiments is necessary to maximize the information collected and minimize the time required while avoiding the injection of systematic biases by the experimenter. Design of experiments (DOE) is the branch of statistics that studies how to optimize the planning of experiments. One of the cornerstones in experimental design is the principle of randomization. This technique ensures that the errors in the experiments will consist of independently distributed random variables [9]. A random sampling of experimental points respects the aforementioned principle but does not efficiently explore the multi-dimensional state space defining the collection of all possible experimental points (attitudes for the wind tunnel experiment). Latin hypercube sampling (LHS) solves this problem by maximizing the variability of the sampled points. Contrary to random sampling, which does not account for previous sampled points, LHS divides each dimension of the N-dimensional state space into M non-overlapping, equal intervals creating a subdivision of M^N hypercubes. It then samples randomly within each hypercube by ensuring that, for each variable, only one sample point is selected from each interval. In this way, Latin hypercube sampling ensures the variability of the experimental points within the whole state space while preserving the randomization requirement. A two-dimensional example of LHS with $N = 2$ and $M = 10$ is presented in Figure 4. It can be noticed how for each sampled point, within the range of the specified intervals, no other points are sampled in the corresponding row or column.

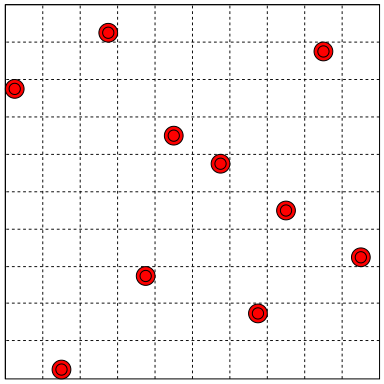

Figure 4: Two-dimensional example of Latin Hypercube Sampling.

4.2 Model Structure Identification

We adopt step-wise linear regression, whose methodology is detailed in the following, to infer the aerodynamic model of the platform from the collected data. However, first, it is useful to define the nomenclature employed in this section. The aerodynamic force and moment components (D,Y,L,M_x,M_y,M_z) represent the dependent variables. The flight parameters α, β, the control parameters δ_e, δ_a and the dynamic parameters ω_x, ω_y, ω_z are the independent variables.

Step-wise regression: For each force and moment model, the independent variables are ranked from the most to the least correlated to the corresponding dependent variable. Based on this ranking, we progressively add regressors to the model increasing as a result the corresponding coefficient of determination R^2 of the model. This coefficient indicates, with a value comprised between 0 and 1, which percentage of the output variable the built model is able to reconstruct.

5. Results

5.1 Platform Aerodynamics Experimental Results

The performed experiments can be classified into two classes: static and dynamic. During a static experiment, each desired attitude is retained for a set amount of time whereas in dynamic experiments the trajectory is continuously evolving. As a result, the former provides less noisy estimates while the latter represents a situation closer to real flight conditions.

DOI: 10.13009/EUCASS2023-585

5.1.1 Static Experiments

Static experiments are conducted to analyze the steady-state aerodynamic response of the UAV platform for fixed attitudes. These experiments require a sufficient elapsed time at each attitude in order to ensure that the transient effects have settled. The transient time is defined as the duration starting from when a new attitude is achieved until the steady state condition is established. To achieve this, we choose a wait time of three seconds for each attitude. This duration allows for the passage of the transient time and enables the collection of a buffer of steady-state data which is crucial for filtering out platform vibrations that may be present. Due to the inherent challenges in generating a completely laminar, uniform, and constant airflow using the Windshaper in an open space, physical vibrations of the platform can occur. Consequently, the advantage of this type of experiment is that it provides a dataset with reduced noise, enabling a more accurate fitting of the data. The reference attitudes tested in this study were sampled using Latin hypercube sampling, as illustrated in Figure 5, which ensures a well-distributed and representative selection of attitudes for analysis while minimizing the number of samples needed to explore the state-space.

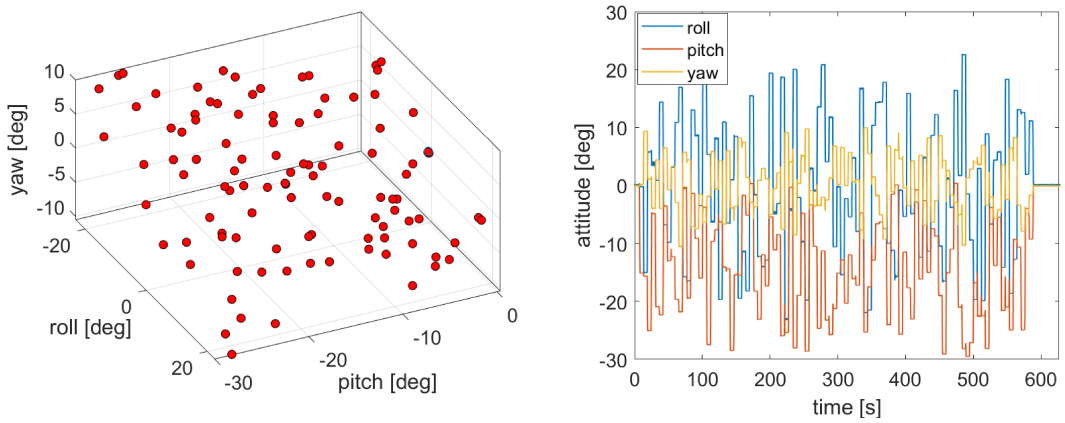

Figure 5: Data sampling for static experiment reference attitudes.

The results of these experiments are depicted for the longitudinal dynamics in Figure 6.

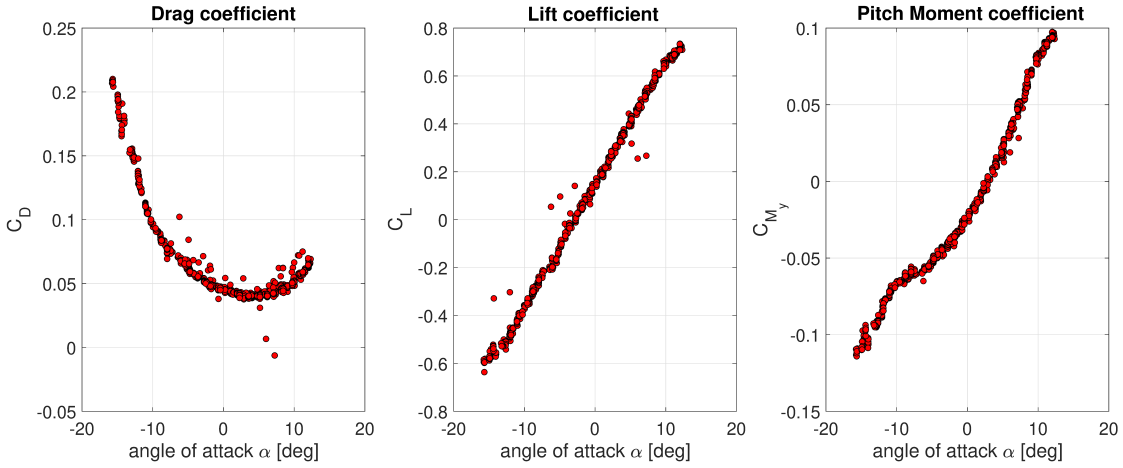

Figure 6: Longitudinal dynamics for static experiments.

It can be noticed that the curves in Figure 6 exhibit a low level of noise, as they represent the steady-state behavior and filter out the physical vibrations of the examined platform. Of particular interest is the observed positive correlation between the angle of attack and the pitching moment. This relationship indicates that the UAV under investigation is statically unstable, requiring active control surface deflection to achieve stability during flight. This instability arises due to the relative distance between the neutral point and the center of gravity, with the former located ahead of the latter. As a result, the UAV is more easily disturbed by external conditions (e.g. gusts of wind) but at the same time more maneuverable with faster responsiveness to control commands, making it highly agile.

DOI: 10.13009/EUCASS2023-585

5.1.2 Dynamic experiments

While static experiments provide a less noisy dataset, they neglect the effects of flight dynamics and how it actually impacts the airflow distribution around the UAV. In this context, dynamic experiments supply a more truthful representation of real flight condition.
The primary objective of dynamic experiments is to investigate the effects of various dynamics on the attainment of the same attitude. This is accomplished by employing Lissajous curves, which are a superposition of oscillations with different angular frequencies, enabling the description of complex harmonic motion. To design a dynamic experiment, we construct roll, pitch, and yaw trajectories as sequences of harmonic curves, with their parameters determined using Latin hypercube sampling. By combining these harmonic sequences, we can define Lissajous curves that describe a complex trajectory in three-dimensional space. The resulting attitude components are shown in Figure 7.

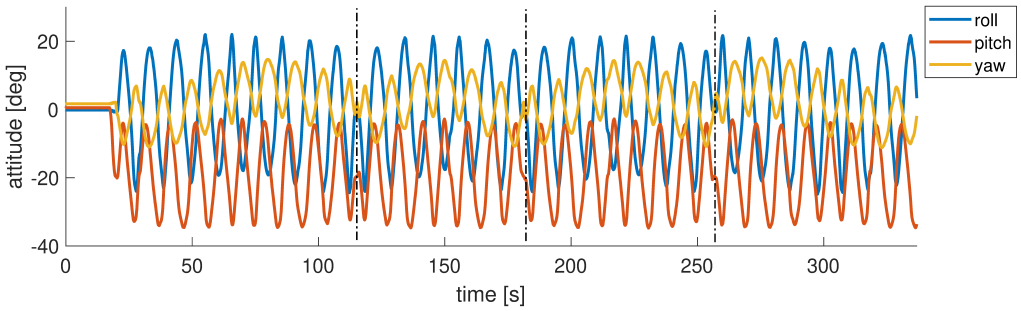

Figure 7: Reference attitudes for dynamic experiments.

To evaluate the influence of flight dynamics magnitude, we conducted a dynamic experiment by manipulating the speed of the robotic arm. The experiment was repeated twice, with the robotic arm speed set at 10% and 30% of its maximum capability. In order to facilitate comprehension and analysis, Figure 8 illustrates the lift coefficient as a function of the angle of attack for a single period of the Lissajou curves.

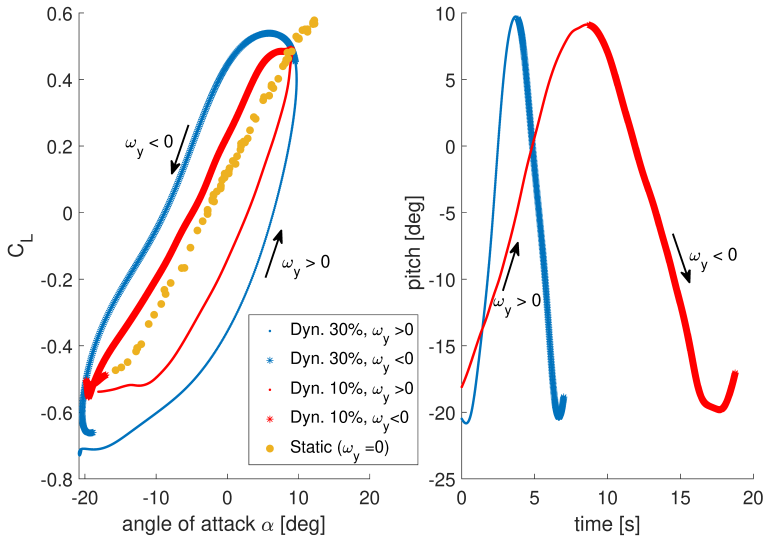

Figure 8: Robot arm speed impact on lift curve.

The dynamic experiment results are compared with those of the static experiment. It is evident that the effects of flight dynamics transforms the curve observed under static conditions. Specifically, a positive ω_y causes a downward shift in the lift curve, while a negative ω_y causes an upward shift.
The visualization presented represents a two-dimensional projection of a three-dimensional plot. The static curve corresponds to a slice of the 3D surface for $\omega_y = 0$, whereas the dynamic curve describes a surface contour in the 3D plane, flattened in the 2D plane. However, it should be noted that this visualization only depicts an isolated experiment aimed at proving the observability and noise characteristics of the acquired data.

DOI: 10.13009/EUCASS2023-585

In the complete experiments, the objective is to stimulate all variables simultaneously, making it challenging to visualize individual effects in isolation. Figure 9 illustrates the output of the comprehensive dynamic experiment, which is employed to determine the model structure and its coefficients.

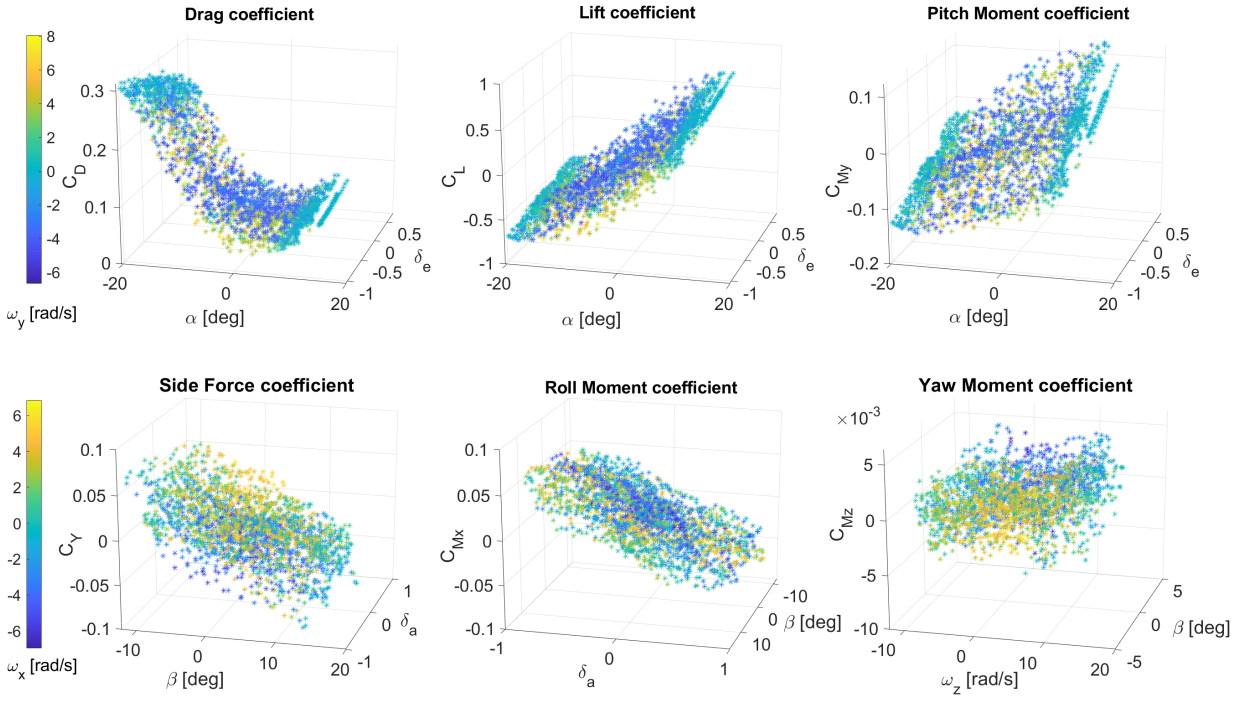

Figure 9: Full dynamics experimental data.

5.1.3 Reyonlds Number Effect

Table 1 shows the ranges of Reynolds number for the considered delta-wing ($\bar{c} = 0.26m$) for a variety of air density ($\rho \in [0.9; 1.2] Kg/m^3$) and temperature ($T \in [0°; 35°] C$) values.

Table 1: Reynolds number values for the flight speed range

Flight speed	**Reynolds number range**
$V = 10m/s$	$Re \in [1.2; 1.8] \times 10^5$
$V = 15m/s$	$Re \in [1.8; 2.7] \times 10^5$
$V = 20m/s$	$Re \in [2.4; 3.6] \times 10^5$

The Reynolds number effect is analysed with static experiments at different reference airspeeds spanning from 60% to 100% of the Windshaper maximum velocity output ($V_{max} = 11.3\ m/s$).
Figure 10 depicts the impact of Reynolds number on the drag and lift coefficient curves. The drag coefficient curve shows minimal impact across most of the tested angle of attack range. This is in accordance with [11], which presents an extensive study for airfoil aerodynamic characteristics for Reynolds numbers in the [60 000 300 000] range and reports qualitatively similar airfoil drag polar for Reynolds numbers superior to 100 000 which is this study's case as per Table 1. On the other hand, the effect of the Reynolds number on the lift curve is more evident. The change in the slope denotes a relatively higher lift produced at higher Reynolds number for the same angle of attack. This observation aligns with the results obtained in [12], which investigated the aerodynamics of an unpowered fixed-wing MAV (Micro Aerial Vehicle). The stall angle remains consistent at 14 degrees irrespective of the Reynolds number. Nevertheless, it is worth noting that the typical angle of attack range considered for delta-wing flight (3-10 degrees) is minimally affected. Therefore, this effect is deemed negligible during the current phase of aerodynamic identification.

DOI: 10.13009/EUCASS2023-585

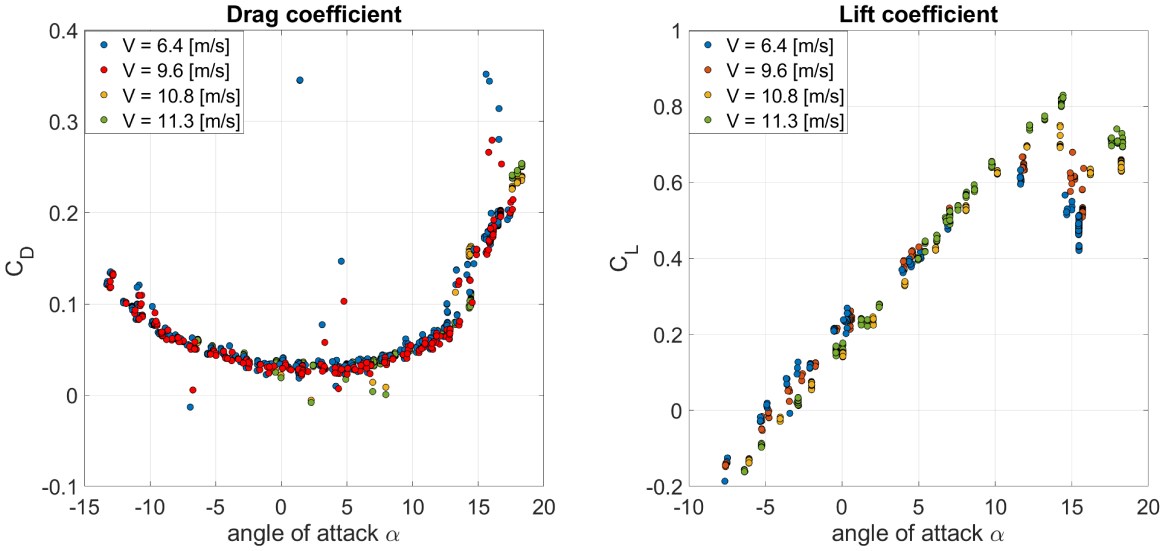

Figure 10: Impact of different Reynolds numbers on drag and lift coefficient curves

5.2 Model Fitting

As introduced in Section 4, stepwise regression, which allows to rank each parameter contribution to the coefficient of determination R^2, is employed to construct the model structure. However, it is important to note that maximizing this coefficient does not always result in a better model, as it can potentially lead to overfitting by fitting the noise instead of the underlying signal. Using this methodology, several models fitting the data at different levels of complexity can be generated. Here are presented the results of a simple model, only accounting for the main contributors for each force and moment component. The model structure is as follows:

$$C_D = C_{D0} + C_{D\alpha}\alpha + C_{D\alpha 2}\alpha^2 \tag{11}$$
$$C_Y = C_{Y0} + C_{Y\beta}\beta \tag{12}$$
$$C_L = C_{L0} + C_{L\alpha}\alpha \tag{13}$$
$$C_{Mx} = C_{Mx0} + C_{Mx\delta_a}\delta_a \tag{14}$$
$$C_{My} = C_{My0} + C_{My\alpha}\alpha + C_{Mx\delta_e}\delta_e \tag{15}$$
$$C_{Mz} = C_{Mz\delta_a\delta_e}\delta_a\delta_e \tag{16}$$

By focusing on the primary factors influencing each force or moment component, we aim to capture the essential features of the system while avoiding unnecessary complexity.

5.3 Propulsion System Experimental Results

In this section, we present the analysis of the experimental data collected during the open-wind tunnel experiments for the propulsion system. The aim is the identification of the propulsion system coefficients presented in Eq. 8 and 9. The experiments consist in measuring the thrust T and torque Q produced by the propeller at different airflow velocities generated using the Windshaper. The robotic arm remains static during the data acquisition, with zero pitch, yaw, and roll. The raw data obtained from the experiments has undergone necessary calibration to eliminate the force contributions from gravity, as described in Section 4. Additionally, prior to parameter regression, the data has been subjected to low-pass filtering to remove zero mean signals, such as physical vibrations, and load-cell sensor noise. Figure 11 depicts the relationship between the throttle command provided by the experimenter and the corresponding measured propeller speed at the output.

DOI: 10.13009/EUCASS2023-585

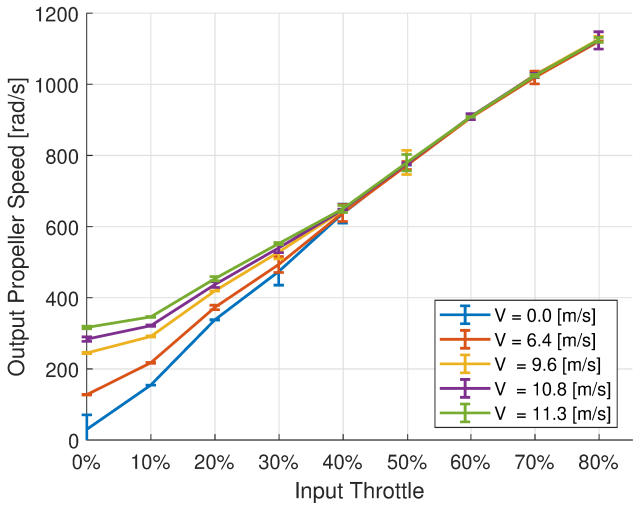

Figure 11: Measured propeller speeds for experimental input throttle and arispeed ranges.

Notably, the chosen reference airspeeds exhibit an influence on the measured propeller speed. In the presence of external airflow, a fixed pitch propeller starts to spin due to *windmilling* [1]. Consequently, the measured propeller speed will be influenced by the airflow-driven windmilling phenomenon when lower desired propeller speeds are requested. This effect gradually diminishes in significance as the throttle input increases, ultimately ceasing when the propeller accelerates the air mass beyond the reference airspeed. To establish a model for the propulsion system, we employ equations 8 and 9 to fit the experimental data. Figure 12 depicts the fitting of the data to the thrust and torque models, respectively.

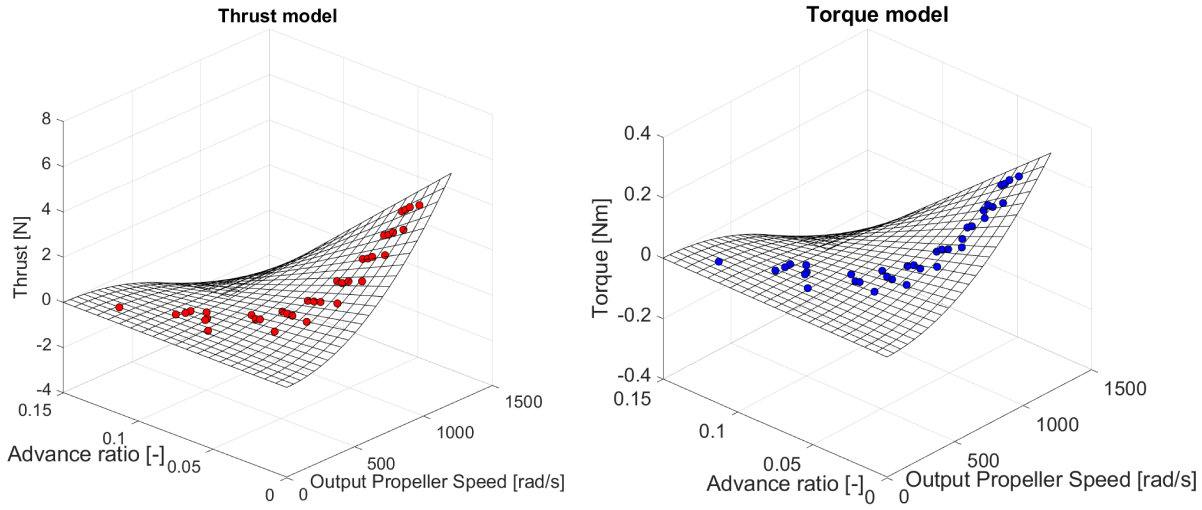

Figure 12: Thrust and torque models fitted to experimental data.

It clearly demonstrates that the proposed model structure accurately captures the distribution of the experimental data. The corresponding model parameters can be found in Table 2.

Table 2: Thrust and torque model parameter values

	CT0	**CT1**	**CQ0**	**CQ1**
Values	$+3.52 \cdot 10^{-6}$	$-3.48 \cdot 10^{-5}$	$+8.68 \cdot 10^{-8}$	$-9.61 \cdot 10^{-7}$

To validate the effectiveness of our model, we compare the predicted thrust and torque signals with the raw and filtered reference data for various throttle values. Figure 13 presents these comparisons, illustrating the agreement

DOI: 10.13009/EUCASS2023-585

between the predicted signals and the reference data.

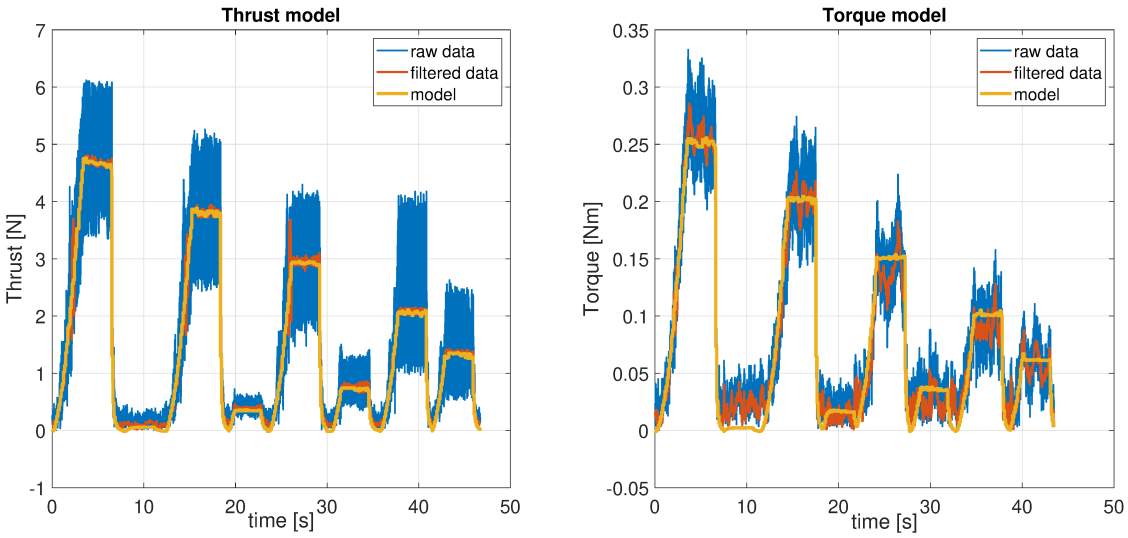

Figure 13: Comparison of model prediction on thrust and torque with raw and filtered data.

It can be noticed that in some conditions the load cell measures are susceptible to significant noise, in particular for the torque, as the values produced are small in magnitude and the signal-to-noise ratio is reduced. In such instances, relying on the proposed simplified model may prove to be a reliable enough solution for navigation purposes while only depending on relative airspeed and propeller speed information.

5.3.1 Propeller-Body Mutual Interaction

In this section, we investigate the interaction between the UAV body and the propeller blade when subjected to an airstream. The previous experiments, described in Section 5.3, were conducted with the propeller mounted on the drone, accounting for the influence of the UAV body on propeller efficiency in the propulsion system model parameters identification phase. However, the effect of a spinning propeller on the airflow around the UAV body, known as the propwash effect and introduced in Section 2.4.2, has not been considered yet.
We evaluated the impact of propeller speed on the UAV drag and lift coefficients using the experimental data collected during the propulsion system aerodynamic characterization. Figure 14 illustrates the results and reports the effects in terms of aerodynamic efficiency (C_L/C_D) variation. Because of propeller windmilling at lower motor RPMs, these data are discarded and therefore are not shown.

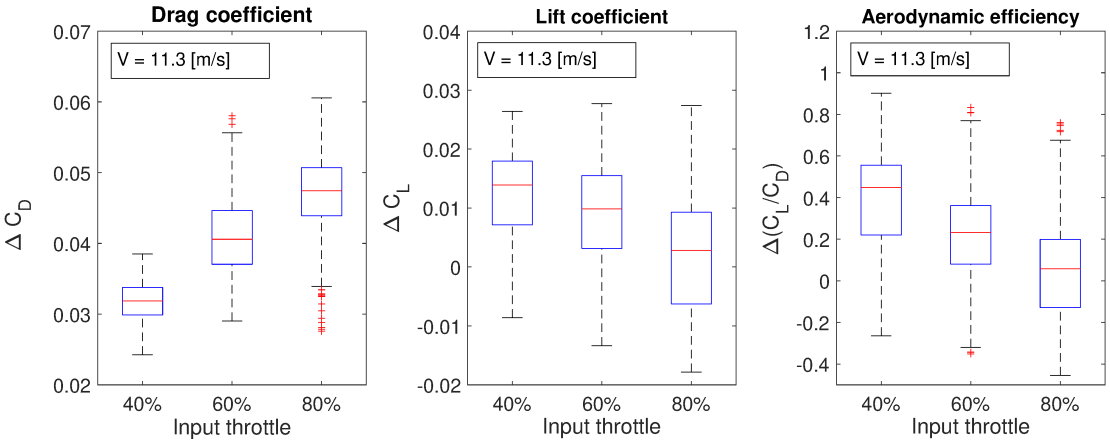

Figure 14: Propwash effect on draf coefficient, lift coefficient and aerodynamic efficiency.

Notably, both the UAV drag and lift coefficients result increased due to propeller's influence on the upstream airflow. However, the drag coefficient grows proportionally with the output propeller speed, while the lift coefficient

DOI: 10.13009/EUCASS2023-585

increase is maximized at a specific propeller speed value before degrading again. The boxplots indicate that the propwash effect on lift exhibits less statistical significance compared to its impact on drag. In terms of aerodynamic efficiency, we found a slight improvement for propeller speeds in the middle range.

5.4 Model-based Navigation Results

The functional model based on the platform and propulsion system aerodynamic characterization presented in the previous sections are tested using an offline implementation of the proposed model-based navigation filter whose general architecture has been presented in Section 2.2. Navigation data are obtained from a real test flight of the delta-wing UAV. The open-source PixHawk autopilot (FMUv5) has been used with its barometer and one of its MEMS IMU, data of which are recorded together with control-command and GNSS positions. Although implemented in replay, the filter provided solution is such as would be obtained in real time. GNSS outages are reproduced by withholding GNSS observations within the filter. The model-based navigation solution is evaluated by how closely it follows the reference navigation solution. The reference is the traditional kinematic solution of the onboard autopilot navigation filter that would be obtained without absence of GNSS signal. The evolution of the horizontal error in time is depicted for an outage of 210 seconds in Figure 15.

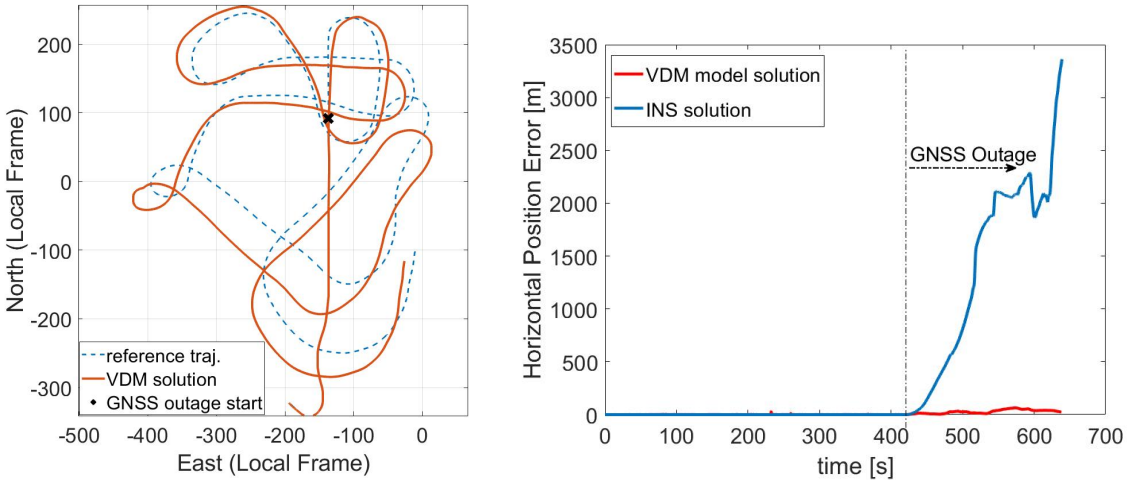

Figure 15: Horizontal position error for GNSS denied navigation.

In accordance to simulation [6] and experimental results [7], [8] on other platforms, model-based navigation for a delta-wing UAV demonstrates a significant improvement in positioning error in GNSS denied scenarios.

6. Conclusions & Perspectives

In conclusion, this work presents a systematic procedure for aerodynamic characterization and a practical model-based solution for reliable navigation during GNSS outages specifically tailored for a delta-wing UAV. It provides a detailed description of the procedure to be followed for characterizing the aerodynamics of a delta-wing UAV using an open wind tunnel set-up, outlining the steps involved in the experimental process. The presented methodology focuses on optimizing flight parameters observability for time constrained experiments through a well-designed set of experiments. Additionally, the study examines the influence and statistical significance of secondary aerodynamic factors such as propwash and Reynolds number effects. The conducted experiments yield valuable data that allow the derivation of a simple yet accurate model for the UAV's aerodynamics. The improvement in navigation performance is evaluated empirically in-flight using an offline implemented navigation solution, notably relying solely on data collected from low-cost sensors embedded in a commercially available autopilot. The obtained results clearly demonstrate the efficacy of the model-based navigation solution during GNSS outages. The model-based approach outperforms the conventional INS-GNSS navigation, yielding a significantly smaller positioning error. This highlights the potential of model-based navigation in enhancing the accuracy and reliability of UAV navigation systems in challenging situations. It is worth noting that while the simplified model defined by equations (11)-(16) provides valuable applicability, it may not capture the full complexity of the system. Future analysis should focus on determining the optimal compromise between model

DOI: 10.13009/EUCASS2023-585

structure simplicity and navigation accuracy under GNSS outage scenarios, further refining and enhancing the proposed model-based navigation solution.

7. Acknowledgments

The author would like to express his sincere gratitude to Dr. W. Stewart and the LIS laboratory for providing the experimental facility availability and helping in setting up the experiments. Dr. I. Doytchinov and S. Reading for their help in the experiment design and finally E. Chelly for his contribution in this study's data collection.

References

[1] E.M. Coates, A. Wenz, K. Gryte, and T.A. Johansen. Propulsion system modeling for small fixed-wing uavs. In *2019 International Conference on Unmanned Aircraft Systems (ICUAS)*, pages 748–757, 2019.

[2] M. Figat and P. Piatkowska. Numerical investigation of mutual interaction between a pusher propeller and a fuselage. *Proceedings of the Institution of Mechanical Engineers, Part G: Journal of Aerospace Engineering*, 235, 06 2020.

[3] G.Laupré, P. Longobardi, J. Skaloud, and J-C. Charlaix. Model based navigation of delta-wing uav-in-flight calibration and autonomous performance. *European Journal of Navigation*, 21(1):22–30, 2021.

[4] A. Gupta, P.A. Narayana, and G. Ramesh. Effect of turbulence intensity on low reynolds number airfoil aerodynamics. *International Journal of Engineering and Technology*, 7, 2017.

[5] Kwanchai K. Chinwicharnam and C. Thipyopas. Comparison of wing-propeller interaction in tractor and pusher configuration. *International Journal of Micro Air Vehicles*, 8:3–20, 03 2016.

[6] M. Khaghani and J. Skaloud. Autonomous vehicle dynamic model-based navigation for small uavs. *Navigation: Journal of The Institute of Navigation*, 63(3):345–358, 2016.

[7] M. Khaghani and J. Skaloud. Assessment of vdm-based autonomous navigation of a uav under operational conditions. *Robotics and Autonomous Systems*, 106:152–164, 2018.

[8] G. Laupré and J. Skaloud. Calibration of fixed-wing uav aerodynamic coefficients with photogrammetry for vdm-based navigation. In *Proceedings of the 2021 International Technical Meeting of The Institute of Navigation*, pages 775–786, 2021.

[9] D.C. Montgomery. *Design and Analysis of Experiments, 8th Edition*. John Wiley & Sons, Incorporated, 2012.

[10] F. Noca, G. Catry, N. Bosson, L. Bardazzi, S. Marquez, and A. Gros. *Wind and Weather Facility for Testing Free-Flying Drones*. 2019.

[11] M. Selig, J.J. Guiglielmo, A.P. Broeren, and P. Giguere. *Summary of Low-Speed Airfoil Data*, volume 1. SoarTech Publications, 1995.

[12] C. Thipyopas and N. Intaratep. Aerodynamics study of fixed-wing mav: Wind tunnel and flight test. In *International Micro Air Vehicles conference 2011 summer edition*, 2011.

[13] L.W. Traub. Effect of a pusher propeller on a delta wing. *Aerospace Science and Technology*, 48:115–121, 2015.

[14] L.W. Traub, B. Moeller, and O. Rediniotis. Low-reynolds-number effects on delta-wing aerodynamics. *Journal of Aircraft - J AIRCRAFT*, 35:653–656, 07 1998.